Nuclear Materials and Energy 36 (2023) 101495

Contents lists available at ScienceDirect

Nuclear Materials and Energy

journal homepage: www.elsevier.com/locate/nme

In situ study of thermal shock damage to high-temperature ceramics

D.E. Cherepanov [a,b,*], L.N. Vyacheslavov [a], V.A. Popov [a,b], G.A. Ryzhkov [a], A.A. Kasatov [a,b], A.A. Vasilyev [a], A.S. Arakcheev [a], A.A. Ruktuev [a,c], I.V. Kandaurov [a], A.A. Shoshin [a,b]

[a] Budker Institute of Nuclear Physics SB RAS, Novosibirsk, 630090, Russia
[b] Novosibirsk State University, Novosibirsk, 630090, Russia
[c] Novosibirsk State Technical University, Novosibirsk, 630073, Russia

ARTICLE INFO

Keywords:
Boron carbide
Plasma-facing components
Laser heating
High-temperature ceramics
In situ diagnostics
Thermal shock

ABSTRACT

New generations of fusion devices need alternative plasma-facing materials. The currently approved material composition for the first wall and divertor of the ITER tokamak has a number of disadvantages: insufficient resistance to thermal shock, sputtering of microparticles into plasma and high atomic number Z of the armor material. A promising but largely untested idea is the proposal to use high-temperature ceramics as armor materials for the most heat-loaded plasma-facing components of new-generation fusion devices. Among the advantages of ceramics are the low Z and high enough resistance to intense heating. More research is needed that would help to understand how the material withstands high heat fluxes during transient plasma events. This work is devoted to the description of an experimental method that makes it possible to estimate the critical temperature at which the damage of ceramics begins as a result of a thermal shock of submillisecond duration. As a demonstration of the efficiency of the method, the critical temperature for hot pressed B_4C under thermal shock was determined: its value was about 1200–1400 K.

1. Introduction

High-temperature ceramics are promising alternative materials for the role of a protective coating for plasma-facing components (PFCs) of a magnetic fusion device. Among the advantages of ceramics over other materials in this case, one can note a low Z and high resistance to intense heating. For example, at present, tungsten is considered to be the most suitable material for manufacturing the divertor armor and some plasma-facing components in tokamaks. However, this metal is not an ideal candidate due to recrystallization [1,2], the brittle-ductile nature of thermal deformation [1,3] and high Z. For this reason, the search for the best alternative material for the manufacture of the first wall and the divertor of tokamaks does not stop.

Attempts have been made to use high-temperature ceramics to manufacture plasma-facing components [4–8]. Among the most suitable materials for this role are silicon carbide (SiC), boron carbide (B_4C) and MAX-phase (Ti_3SiC_2). Indeed, these materials and composites based on them are highly resistant to thermal shock [9–12]. There are approaches that can significantly reduce hydrogen retention or help to remove hydrogen from SiC and B_4C [13,14]. In terms of gamma and neutron radiation protection, B_4C is one of the best materials [15]. For this reason, it is approved for the manufacture of protection for ITER tokamak port plugs [16,17]. There are also methods to improve this property [18].

One of the key properties of the armor material of the PFC is its resistance to thermal shocks produced by the plasma during the operation of the fusion device. B_4C has already been considered as a material for PFC protection of tokamaks and stellarators [6–8]. However, studies that would allow us to evaluate the resistance of this material and other high-temperature ceramics to thermal shock, which corresponds to that in the case of ELMs [19], are not enough. More research is needed to show how B_4C and other promising plasma-facing material (PFM) ceramics are resistant to such events in new-generation facilities like CFETR or DEMO. Thus, the purpose of this work was to develop experimental technique for studying damage to the high-temperature ceramics surface as a result of thermal shock. In more detail, it was necessary to test the possibility of using the approach described in [20–27] to study damage to the surface of high-temperature ceramics. The application of this approach made it possible earlier to observe the motion of a layer of molten tungsten on the surface of a sample [21] and to study the dynamics of the ejection of microparticles from the melt depending on their size and the intensity of thermal shock [23, 24]. Using the *in situ* technique, the trajectories and ejection time of microparticles were recorded, as well as localization of the initial point of emission of microparticles which showed that microparticles escape from overheated sections of the melt [25]. The appearance of overheated areas on a uniformly heated surface of a tungsten sample

* Corresponding author at: Budker Institute of Nuclear Physics SB RAS, Novosibirsk, 630090, Russia.
E-mail address: dmitrii.e.cherepanov@gmail.com (D.E. Cherepanov).

https://doi.org/10.1016/j.nme.2023.101495
Received 31 January 2023; Received in revised form 12 August 2023; Accepted 25 August 2023
Available online 27 August 2023

Table 1
Thermomechanical properties of boron carbide provided by Virial Ltd.

Poisson's ratio σ	Young's modulus E (GPa)	Thermal expansion α (K^{-1}) @ $T \approx 500$ K	Thermal expansion α (K^{-1}) @ $T \approx 1300$ K
0.2	440	$4.5 \cdot 10^{-6}$	$5.6 \cdot 10^{-6}$

is associated with a deterioration in the bond of these areas with the base material due to surface modification by previous thermal shocks [26]. Under transient thermal loads with an intensity below the melting threshold, the dynamics in the roughness of the initially mirror-polished surface of a tungsten sample versus dynamics of surface temperature has been studied [22]. The residual bending of the sample made it possible to estimate the tensile residual stress associated with residual plastic deformations of the surface of tungsten samples heated by thermal shocks [27]. In case the tensile strength of tungsten is exceeded, it leads to cracking of the surface. Cracking occurs at time delay several orders larger than the time required for the surface to cool down to ductile-to-brittle transition temperature (DBTT) [22].

The main advantage of this technique is the possibility of obtaining data on the erosion of test samples directly during the thermal shock. The approach is based on *in situ* recording and analysis of monochromatic radiation scattered by the sample, the change of which indicates the occurrence of erosion processes on the surface. The experimental results should make it possible to determine the critical parameters of heating at which the damage of the irradiated sample surface began. In the course of this work, it was necessary during the B_4C test to adapt the *in situ* technique that allows monitoring the process of damage to the sample surface during pulsed laser heating in order to further apply this approach to study other PFM-promising ceramics. In this paper, we will focus on describing damage to the surface of B_4C due to rapid heating to temperatures below the melting threshold. Damage occurs due to detachment of small volumes of matter. The reasons for this process, as well as its experimental observation, are given below.

2. Sample description

The B_4C sample used in the experiments was produced by Virial Ltd (St. Petersburg) by hot pressing. The hot pressing method makes it possible to obtain ceramics with low porosity, which has a positive effect on its mechanical strength and thermal conductivity. It is expected that the selected sample will have a sufficiently high resistance to thermal shock. It is presented in the form of a $50 \times 50 \times 10$ mm^3 plate. The density is 2.51–2.52 g/cm^3, the content of impurities does not exceed 1% (O: 0–0.18%, Al: 0–0.1%, Si: 0.1–0.21%, Fe: 0–0.13%) [28]. The known thermomechanical properties of the provided sample are shown in Table 1. These values correspond to the characteristic reference data for B_4C [29–31].

The sample surface was preliminarily polished to minimize the fraction of diffusely scattered light. The sample surface microscopy images are shown in Fig. 1, the result of optical profilometry of the surface is presented in Fig. 2. Open pores can be seen with typical size ~ 10 μm.

3. Critical temperature estimation

Let us consider the process of B_4C surface erosion due to the pulsed heating of a small area on the surface. Polycrystalline ceramics contain defects (e.g. pores, grains and inclusions with mechanical properties that differ from average), which are its weak point. With rapid heating of the surface, thermal expansion of the substance occurs, which leads to the appearance of compressive stresses. When the surface is heated, the compressive stresses will be greater in the longitudinal direction relative to the surface plane, since the substance can freely expand in the transverse direction. Such asymmetric pressure on defects will lead to the transition of compressive stresses in one direction into tensile stresses in another direction in the vicinity of the defects [32,33]. When

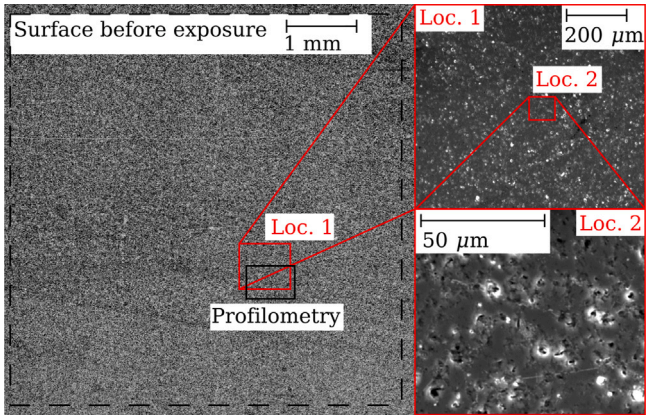

Fig. 1. The unexposed sample surface microscopy images with different magnifications. The left image was obtained using an optical microscope, the right images at high magnifications were obtained using SEM. The location where the surface profilometry data was taken is marked with a black rectangle.

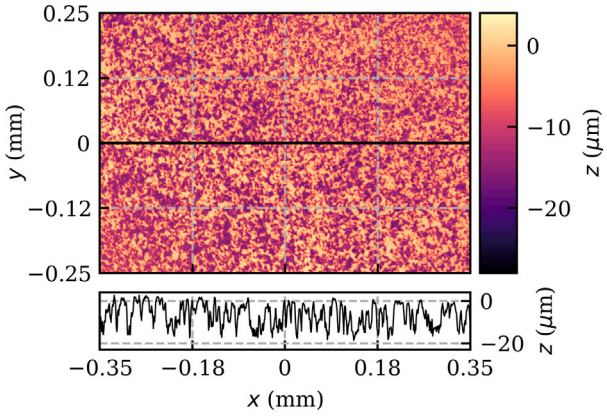

Fig. 2. The result of optical profilometry of the surface of the boron carbide sample before the experiments.

tensile stresses reach the ultimate tensile strength, crack initiation begins, and small volumes of matter are detached from the surface with the formation of craters. Statistically, this process occurs when the compressive stress reaches the compressive strength. It is assumed that such a process limits the operating temperature of the ceramics. Next, we will make a simple estimation of the critical heating temperature at which the described process begins, and then consider the experimental results that make it possible to describe craters formation experimentally using *in situ* diagnostic systems.

The heat diffusion depth λ_h can be estimated as follows:

$$\lambda_h \sim \sqrt{\frac{\varkappa \cdot t}{c_v \cdot \pi \cdot \rho}}, \tag{1}$$

where $\varkappa$ is the thermal conductivity, t is the characteristic heating time, c_v is the specific heat and ρ is the density. For thermal shock with characteristic time $t \sim 1$ ms: $\lambda_h \sim 0.1$ mm $\ll h, r$ (h and r are the sample thickness and characteristic size of the heated area on the surface, respectively). The values $\varkappa$ and c_v are taken from [29, p. 146], $\rho \approx$ $\approx$ 2.51–2.52 g/cm^3. Thus, we can assume that thermal expansion occurs uniformly, and it is permissible to use a one-dimensional approximation

to describe it. The linear density $\rho_s = \int \rho dh$ cannot change, and macroscopically only deformation occurs in the direction of the normal vector. Then, to describe the erosion of the surface of a brittle material, we will use the linear theory of elasticity [34]:

$$\sigma_{\alpha\beta} = -K \cdot 3 \cdot \alpha \cdot \delta T \cdot \delta_{\alpha\beta} + K \cdot u_{\gamma\gamma} \cdot \delta_{\alpha\beta} + 2 \cdot \mu \cdot \left(u_{\alpha\beta} - u_{\gamma\gamma} \cdot \delta_{\alpha\beta}/3\right), \quad (2)$$

where $K = \frac{E}{3(1-2\sigma)}$ is the bulk modulus of elasticity (bulk and compression modulus), $\mu = \frac{E}{2(1+\sigma)}$ – shear modulus, E – Young's modulus, σ – Poisson's ratio, α – coefficient of linear thermal expansion. Eq. (2) is actually matrix equation, so tensor notation is used; α, β, γ are indexes that can be one of x, y, z independently; z is direction normal to surface, x, y are directions in surface; $\delta_{\alpha\beta}$ is Kronecker delta. Einstein summation convention is used, so $u_{\gamma\gamma}$ is trace of strain tensor. According to definition of strain tensor one can see, that

$$u_{\gamma\gamma} = \mathrm{div}\vec{u} = -\frac{\delta\rho}{\rho}, \quad (3)$$

where $\vec{u}$ is displacement vector, $\delta\rho$ - change in the density. For $\sigma_{\alpha\beta} = 0$ we get by substitution into Eq. (2) the following result: trace $u_{\alpha\alpha} = 3 \cdot \alpha \cdot \cdot \delta T$, which means that α is linear expansion, non-diagonal components are zero $u_{\alpha\beta}\big|_{\alpha\neq\beta} = 0$ in force-less case.

In our case as it was mentioned above, averaged displacement can be only in direction normal to surface, so according to definition $u_{\alpha\beta}\big|_{\alpha\neq z} = 0$. Because of symmetry $u_{\alpha\beta} = u_{\beta\alpha}$, so there only one non zero element in displacement tensor – u_{zz}. Therefore there are no off-diagonal elements $u_{\alpha\beta}$, which means that there are no off-diagonal elements $\sigma_{\alpha\beta}$ either. According to mentioned above structure of displacement tensor it can be rewritten as follows $u_{\alpha\beta} = u_{\gamma\gamma} n_\alpha n_\beta$, where n_α – is α component of normal (orthogonal to the surface, with unit length) vector $\vec{n}$.

$$\sigma_{\alpha\beta} = -K \cdot 3 \cdot \alpha \cdot \delta T \cdot \delta_{\alpha\beta} + K \cdot u_{\gamma\gamma} \cdot \delta_{\alpha\beta} + 2 \cdot \mu \cdot u_{\gamma\gamma} \cdot \left(n_\alpha n_\beta - \delta_{\alpha\beta}/3\right) \quad (4)$$
$$= -K \cdot 3 \cdot \alpha \cdot \delta T \cdot \delta_{\alpha\beta} + u_{\gamma\gamma} \cdot \left(\left(K - \frac{2}{3}\mu\right) \cdot \delta_{\alpha\beta} + 2 \cdot \mu \cdot n_\alpha n_\beta\right),$$

which means, that σ has only two independent non zero components σ_{zz} and $\sigma_{xx} = \sigma_{yy}$.

Uniformity in transverse coordinates ($r \gg \lambda$) and proximity to the surface on which $\sigma_{\alpha z} = 0$, allows us to obtain from Eq. (2):

$$\sigma_{zz} = -K \cdot 3 \cdot \alpha \cdot \delta T + u_{\gamma\gamma} \cdot \left(\left(K - \frac{2}{3}\mu\right) + 2 \cdot \mu\right) = 0, \quad (5)$$

$$\sigma_{xx} = -K \cdot 3 \cdot \alpha \cdot \delta T + u_{\gamma\gamma} \cdot \left(K - \frac{2}{3}\mu\right). \quad (6)$$

From Eq. (5) $u_{\gamma\gamma}$ can be found and used to determine σ_{xx}:

$$\sigma_{xx} = \sigma_{yy} = -\frac{E}{1-\sigma} \cdot \alpha \cdot \delta T. \quad (7)$$

Presented theory ends with the first integrity breach. So, craters formation will start when the compressive stress from Eq. (7) reaches the limit $|\sigma_{xx}| = |\sigma_{yy}| = \sigma_{max}$, where σ_{max} is the compressive strength. Thus, the critical temperature change at which craters formation begins is expressed as follows:

$$\delta T_{critical} = \frac{1-\sigma}{\alpha \cdot E} \cdot \sigma_{max}. \quad (8)$$

Hence, for B_4C we obtain: $\delta T_{critical} \approx$ 900–1200 K (E, α, σ values were taken from Table 1 and σ_{max} from [29,30], the range of values for single value theory is obtained because of uncertainty of material properties.). If we assume that the sample is initially at room temperature $T_{room} \approx \approx$ 300 K then the critical temperature is $T_{critical} \approx$ 1200–1500 K. It should be emphasized here, that the coefficients in Eq. (8) should be taken at surface temperature, that adds uncertainty.

4. Experimental setup

The B_4C sample was at room temperature inside a vacuum chamber at a pressure of about 4 Pa. Thermal shocks were simulated using a neodymium laser on silicate glass with pulsed xenon lamp pumping.

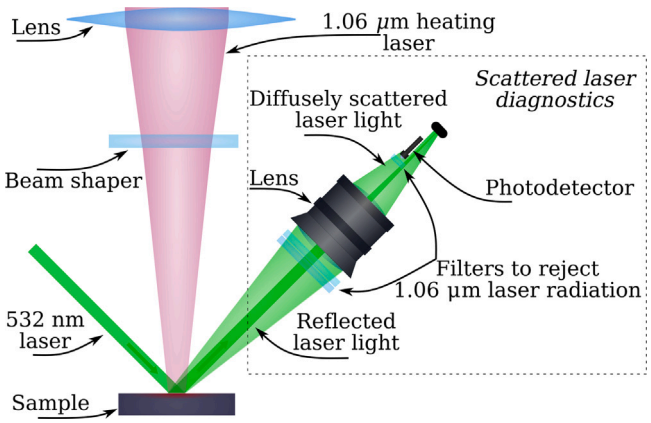

Fig. 3. Scheme of the *in situ* system for the dynamics of damage to the irradiated sample surface diagnostics.

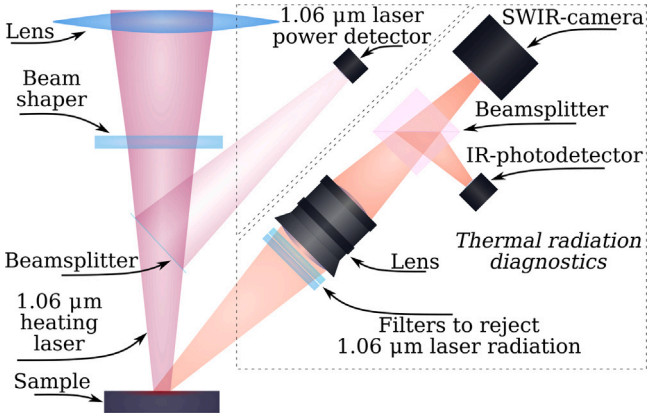

Fig. 4. Scheme of *in situ* system for the thermal radiation of the sample surface diagnostics and 1.06 μm heating laser power detector location.

This laser generates submillisecond pulses at a wavelength of 1.06 μm. The total energy in a pulse can reach 200 J, and by using lenses and beam shapers, it is possible to provide a heat flux to the sample surface up to 10 GW/m^2. This allows to simulate thermal transients during ELMs [26,35].

To monitor the dynamics of surface damage, the diffusely scattered laser radiation at a wavelength of 532 nm was observed. A diagnostic system similar in principle of operation was used for *in situ* studies of tungsten erosion during pulsed electron beam heating [20–22]. Schematic of the experiment with radiant heating paths and diagnostic laser is shown on Fig. 3. To reject the infrared (IR) laser radiation, which heats the sample, a combination of IR-absorbing optical filters and narrow-band 532 nm interference filters was used. Thus, the photodetectors recorded only the radiation of the 532 nm laser. The main limitation of this diagnostic system is the need to preliminary treat the sample surface in such a way that a small amount of diffusely scattered radiation is achieved. In this case, surface erosion leads to a significant increase in the amount of diffusely scattered radiation, and this change can be recorded.

To characterize the heating of the sample, a pyrometric diagnostic system was implemented to estimate the surface temperature, as well as a system that allows recording the power of the heating laser (Fig. 4). The combination of an IR-photodiode and a SWIR-camera makes it possible to monitor the temperature dynamics ($T \gtrsim 800$ K) in a small area on the sample surface and to record the spatial temperature distribution over the surface at a point in time of interest. Determining the temperature based on the thermal radiation of the B_4C surface is

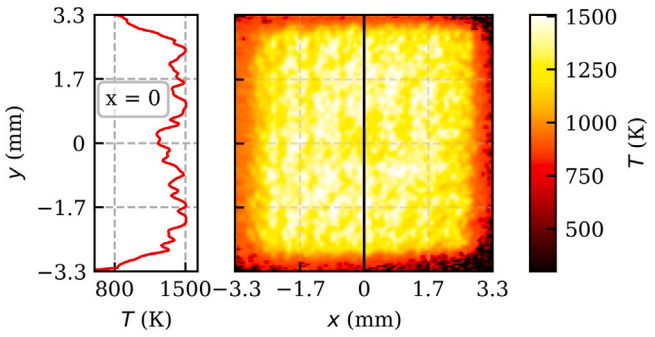

Fig. 5. An example of temperature distribution over the B_4C surface during 1.06 μm laser heating. The graph on the left is plotted along the black line in the 2D temperature distribution on the right.

possible due to the known emissivity in the temperature and wavelength range of interest [36,37]. The pyrometric diagnostic system is also equipped with a combination of absorbing optical filters and a narrow-band notch filter to reject IR radiation from the heating laser.

An example of the temperature distribution over the sample surface during the thermal shock, is shown in Fig. 5. It can be noted that the laser diffuser creates almost uniform heating inside a square $S \approx \approx 6 \times 6$ mm^2 with maximum temperature deviations $\lesssim 20\%$. During the experiment, the diagnostic 532 nm laser illuminates approximately 80% of the heated surface. This means that surface erosion due to overheating occurres simultaneously over a large area, which will significantly affect the fraction of diffusely scattered radiation. Due to this, it is possible to most accurately determine the beginning of the erosion: the signal of the scattered radiation monitoring system quickly begins to grow.

The heating laser power diagnostic system with 1.06 μm radiation detector (Fig. 4) is calibrated to measure the total radiation power to the sample surface $P(t)$. Using the known irradiation surface S, as well as the absorption coefficient of the material, it is possible to estimate the absorbed heat flux W_s. We will assume that all the radiation that is not reflected from the surface goes into heating the sample. Thus, the heat flux can be defined as $W_s(t) \approx (1 - R) \cdot P(t)/S$, where R is the reflection coefficient for the wavelength of 1.06 μm. Let us set $R \approx const$ and estimate the value for B_4C according to the data published in [38] as $R \approx 0.28$.

5. Heat flux factor estimation

For the most complete characterization of the heating of the sample surface, it is most representative to use the heat flux factor F_{hf} [39–41]. In the case of pulsed heating with a constant heat flux $W_s = = const$, the heat flux factor is defined as $F_{hf} = W_s \cdot \sqrt{t}$. However, in the experiments described in this paper, heating is carried out with a non-constant power. To determine the heat flux factor for this case, consider where the definition for the case of constant heating comes from.

Propagation of heat can be simplified to heat equation in the case of small temperature dependence of material thermal properties. Small ratio of heat propagation depth to radius of heating allow to simplify equation to one dimensional $\frac{\partial T}{\partial t} = D \cdot \frac{\partial^2 T}{\partial x^2}$, where $D = \frac{\varkappa}{c_v \cdot \rho}$. Fundamental solution of heat equation is well known: $\Phi = (4 \cdot \pi \cdot D \cdot t)^{-\frac{1}{2}} \cdot e^{-\frac{x^2}{4 \cdot D \cdot t}}$ [42]. Small ratio of heat propagation depth to sample depth allows us to neglect the far boundary and solve equation in half space with boundary condition on heated surface $-\varkappa \cdot \frac{\partial T}{\partial x} = W_s(t)$. After mathematical calculations one can find that surface temperature at $x = 0$ can be calculated as follow:

$$T(t) = \sqrt{\frac{4}{\pi \cdot \varkappa \cdot c_v \cdot \rho}} \int_0^t \frac{W_s(t-\tau)}{2 \cdot \sqrt{\tau}} d\tau \tag{9}$$

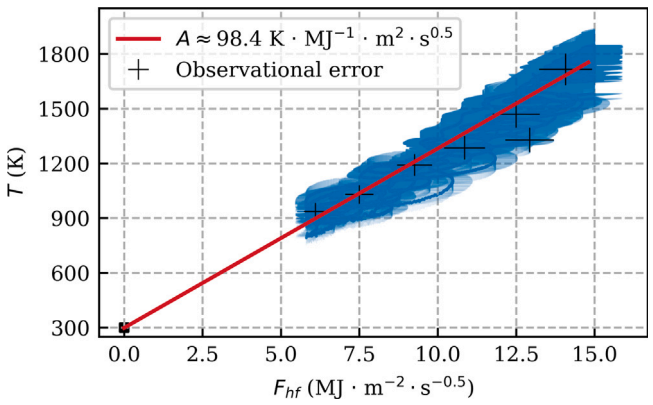

Fig. 6. Experimentally obtained dependence of the surface temperature T of B_4C on the heat flux factor F_{hf} defined according Eq. (10). A line with a slope A is fitted by the least squares method. Observational errors are marked by crosses. Some of the dataset points are highlighted in black for clarity.

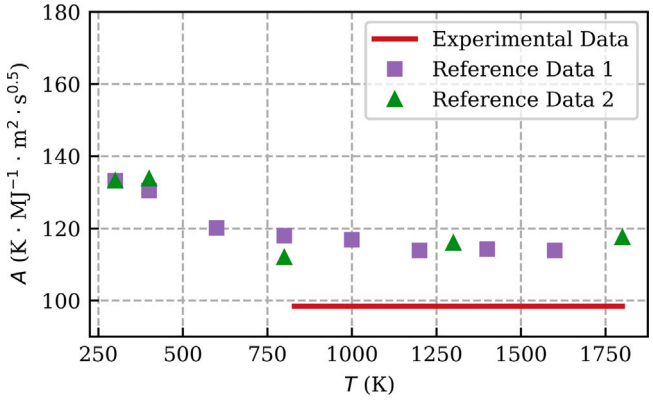

Fig. 7. Experimentally obtained slope of temperature - heat flux factor line A as function of temperature compared to that calculated using the definition $A = \sqrt{\frac{4}{\pi \cdot \varkappa \cdot c_v \cdot \rho}}$, where $\varkappa$ and c_v were taken from reference data (Reference Data 1 from [29], Reference Data 2 from [43]).

So, for the case of non constant time dependence of heat flux $W_s(t)$ surface temperature is proportional to heat flux factor:

$$F_{hf} = \int_0^t \frac{W_s(t-\tau)}{2 \cdot \sqrt{\tau}} d\tau. \tag{10}$$

In case of $W_s(t) = const$ from Eq. (10) we get $F_{hf} = W_s \cdot \sqrt{t}$ as it should be for constant heat flux according to simplified definition formula written above.

To demonstrate the possibility of using such a definition of the heat flux factor (Eq. (10)), let us consider the dependence of T on F_{hf} for the data obtained during the experiments with B_4C presented in Fig. 6. It can be seen that the dependence can be approximated by a linear function: $T = A \cdot F_{hf} + T_{room}$. The slope A of the fitted line must be equal to the $A = \sqrt{\frac{4}{\pi \cdot \varkappa \cdot c_v \cdot \rho}}$ (according to Eqs. (9) and (10)). Let us compare experimentally obtained A with the calculated one based on the known properties of B_4C (Fig. 7) from the reference data [29,43]. The reference data is temperature dependent, while the experimental value of the slope A is constant. It can be seen that the difference is about 20% for $T > 500$ K. This discrepancy is probably due to the fact that for the sample on which the experiments were carried out, such properties as emissivity, absorption coefficient of 1.06 μm laser radiation, thermal conductivity and specific heat are not exactly known. The values for them were taken from the reference data. Nevertheless, such an assessment more fully characterizes the heating of B_4C and

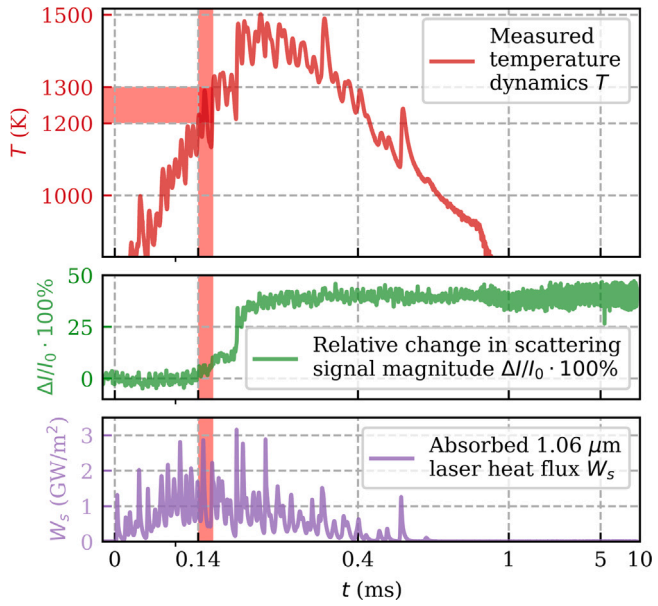

Fig. 8. The result of irradiating a polished sample of B_4C: time dependence of the surface temperature T (red), relative change in the scattered 532 nm laser radiation $\Delta I/I_0 \cdot 100\%$ (green) and absorbed 1.06 μm laser heat flux W_s (purple). From 0 ms to 0.6 ms the graph is made on a linear scale, starting from 0.6 ms on a logarithmic scale. The time interval corresponding to the beginning of the increase in the intensity of diffuse scattering and the interrelated interval of critical temperatures are marked by the intersection of vertical and horizontal red rectangles. (For interpretation of the references to color in this figure legend, the reader is referred to the web version of this article.)

makes it possible to compare the resistance to thermal shock with other materials.

6. Results and discussion

Fig. 8 shows the result of thermal shock of the surface of a B_4C sample. The change in the signal of the scattered radiation monitoring system (green line) occurs due to an increase in the solid angle of the diffusely scattered 532 nm laser. The solid scattering angle in this case can change only as a result of damage to the surface of the sample: when the critical temperature is reached, the material erosion begins. Fig. 8 shows that when the surface temperature reaches 1200–1300 K ($t \approx 0.14$–0.16 ms), the fraction of scattered radiation begins to increase. The growth of the signal continues until the maximum surface temperature is reached, and then the signal becomes constant.

Microscopy images of the sample surface after irradiation with the 1.06 μm laser pulse are shown in Fig. 9. The formation of small craters over the entire irradiated surface is clearly visible. Cavities on the surface shown in Fig. 9, which are much larger than the open pores on the unexposed surface (Fig. 1), are considered as craters. It is as a result of craters formation that the 532 nm laser radiation diffusely scattered by the sample surface increased. Profilometry data shown in Fig. 10 support the microscopy data on craters formation.

To demonstrate the statistical confirmation of the result, Fig. 11 shows the dependence of the relative change in the 532 nm laser radiation diffusely scattered by the sample $\Delta I/I_0 \cdot 100\%$ on the surface temperature T and heat flux factor F_{hf} at the heating stage for 5 experiments. Each experiment was carried out on a pristine unexposed area of the sample surface. The data allow us to conclude that the temperature range 1200–1400 K (marked with a red rectangle) corresponding to the beginning of the signal growth is the critical temperature at which erosion of the heated surface occurs. This agrees well with the estimate according to Eq. (8), given that the sample is initially at room temperature ($T_{critical} \approx 1200$–$1500$ K). The experimentally determined critical

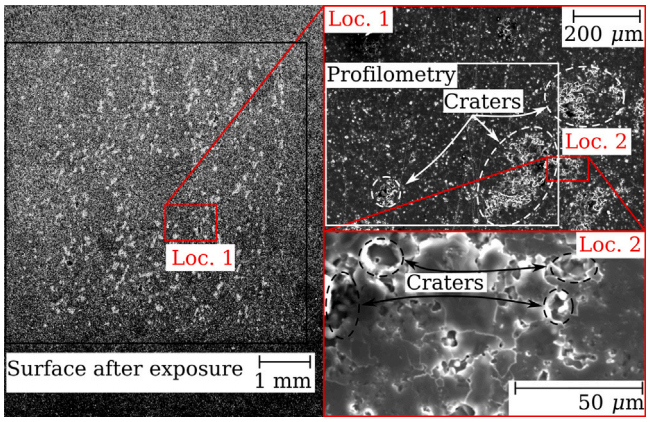

Fig. 9. Microscopy images of the sample surface after irradiation with different magnifications. The left image was obtained using an optical microscope, the right images at high magnifications were obtained using SEM. The area for which profilometry data were obtained is marked with a white rectangle.

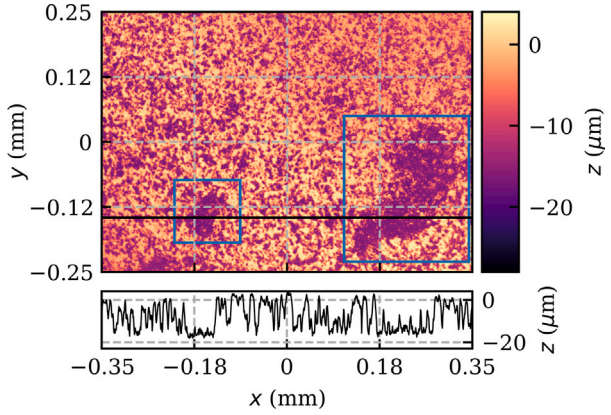

Fig. 10. The result of optical profilometry of the surface of a boron carbide sample after thermal shock. Craters are marked with blue rectangles. (For interpretation of the references to color in this figure legend, the reader is referred to the web version of this article.)

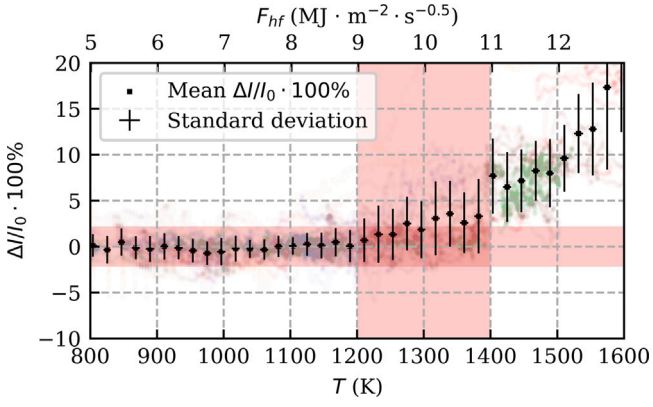

Fig. 11. Dependence of the relative change in the 532 nm laser radiation diffusely scattered by the surface of B_4C on the surface temperature and heat flux factor at the heating stage for 5 experiments. The expected critical temperature and heat flux factor range is marked with a red rectangle. (For interpretation of the references to color in this figure legend, the reader is referred to the web version of this article.)

temperature range is reached when the surface is heated with a heat flux factor of $F_{hf} \approx 9$–11 MJ m^{-1} s$^{-0.5}$ (calculated according Eq. (10)). It should be noted that the above temperature range corresponding to the

beginning of damage to a given material refers to single impacts and the initial room temperature of the sample. The effects of thermal cycling, stationary heating and increased initial temperatures are expected to be investigated in the future.

Let us compare the data obtained with the heating parameters that limit the use of tungsten as PFM. The process that significantly limits the working temperature of tungsten is recrystallization. The recrystallization temperature of tungsten is in the range of 1200–1800 K [44, 45], which is close to the temperature range corresponding to the onset of B_4C erosion. However, characteristic temperatures alone are not enough to draw conclusions about the resistance of the material to pulsed heating, and it is more correct to compare the heat flux factors corresponding to the onset of erosion. The heat flux factor $F_{hf} \approx$ 9–11 MJ m^{-1} s$^{-0.5}$ at which B_4C surface reaches 1200–1400 K is almost two times lower than the tungsten cracking threshold ($F_{hf} \approx \approx$ 23 MJ m^{-1} s$^{-0.5}$ [41], $F_{hf} \approx$ 12–24 MJ m^{-1} s$^{-0.5}$ [46]). According to the results of work [44], in the case of multiple heating pulses, tungsten recrystallization occurs when the heat flux factor in each pulse reaches $F_{hf} \approx$ 15.4–24.7 MJ m^{-1} s$^{-0.5}$. The heat flux factor at which erosion of the B_4C surface begins is approximately half the characteristic limiting heat flux factor during pulsed heating of tungsten. The main reason for the rapid heating of B_4C is the relatively low thermal conductivity. This is a rather serious problem of this material in some cases while in other situation like in sacriefied limiters the low thermal conductivity can protect the cooling pipes from overheating and avoid a potential Loss Of Coolant Accident inside the DEMO vessel [47]. The low Z of the material is also beneficial since any impurities eroded from a limiter made of B_4C will have less effect on the plasma core.

7. Conclusions

The main result of the work is to demonstrate the possibility of using an *in situ* technique based on the analysis of laser radiation scattered by the surface of ceramics to study erosion processes during pulsed heating. The *in situ* experimental results made it possible to determine the parameters of heating the surface of hot pressed B_4C, at which the processes of craters formation begin. *Post mortem* microscopy images and profilometry data showed that, as a result of pulsed heating to temperatures below the melting threshold, craters are actually formed on the surface of the sample. Surface damage begins in the case of rapid heating of the surface to critical temperatures in the range of 1200–1400 K at an initial sample temperature of $T_{room} \approx$ 300 K. This temperature range corresponds to the estimate made in the course of the theoretical description of the process. The heat flux factor at which the critical temperature range is reached during pulsed heating was also estimated: it is almost two times lower than the characteristic limiting heat flux factor during pulsed heating of tungsten.

The approach described in this paper is planned to be used to study other PFM-promising high-temperature ceramics: such as monolithic hot pressed SiC, CVD SiC, SiC/SiC composites, boron-based ceramics and MAX-phases (e.g. Ti_3SiC_2). These materials are of interest due to their high resistance to thermal load, as well as relatively high thermal conductivity compared to other high-temperature ceramics. The authors believe that the approach described in this paper will help to characterize the possibility of using high-temperature ceramics for the manufacture of coatings of plasma-facing components of fusion devices in terms of their resistance to thermal shocks that occur in the case of transient processes during the magnetic plasma confinement. The *in situ* technique described in this paper makes it possible to obtain data on the critical pulsed heating of ceramics. This information will help to understand the limitations in the case of using ceramics as PFM: to estimate the ultimate heating parameters at which erosion occurs.

CRediT authorship contribution statement

D.E. Cherepanov: Methodology, Formal analysis, Investigation, Data curation, Visualisation, Writing – original draft. **L.N. Vyacheslavov:** Project administration, Supervision, Conceptualization, Methodology, Writing – review & editing. **V.A. Popov:** Validation, Formal analysis, Software, Writing – original draft, Writing – review & editing. **G.A. Ryzhkov:** Investigation, Software, Formal analysis, Data curation. **A.A. Kasatov:** Investigation, Software, Formal analysis, Data curation, Validation, Writing – review & editing. **A.A. Vasilyev:** Conceptualization, Validation. **A.S. Arakcheev:** Methodology, Validation, Formal analysis. **A.A. Ruktuev:** Resources, Formal analysis. **I.V. Kandaurov:** Resources, Methodology, Writing – review & editing. **A.A. Shoshin:** Resources, Writing – review & editing.

Declaration of competing interest

The authors declare that they have no known competing financial interests or personal relationships that could have appeared to influence the work reported in this paper.

Data availability

No data was used for the research described in the article.

References

[1] J. Linke, J. Du, T. Loewenhoff, G. Pintsuk, B. Spilker, I. Steudel, M. Wirtz, Challenges for plasma-facing components in nuclear fusion, Matter Radiat. Extrem. 4 (5) (2019) 056201, http://dx.doi.org/10.1063/1.5090100.

[2] A. Durif, M. Richou, G. Kermouche, M. Lenci, J.-M. Bergheau, Impact of tungsten recrystallization on ITER-like components for lifetime estimation, Fusion Eng. Des. 138 (2019) 247–253, http://dx.doi.org/10.1016/j.fusengdes.2018.11.003, URL https://www.sciencedirect.com/science/article/pii/S0920379618307026.

[3] A. Arakcheev, D. Skovorodin, A. Burdakov, A. Shoshin, S. Polosatkin, A. Vasilyev, V. Postupaev, L. Vyacheslavov, A. Kasatov, A. Huber, P. Mertens, M. Wirtz, C. Linsmeier, A. Kreter, T. Löwenhoff, L. Begrambekov, A. Grunin, Y. Sadovskiy, Calculation of cracking under pulsed heat loads in tungsten manufactured according to ITER specifications, J. Nucl. Mater. 467 (2015) 165–171, http://dx.doi.org/10.1016/j.jnucmat.2015.09.034, URL https://www.sciencedirect.com/science/article/pii/S0022311515302233.

[4] J. Coburn, E. Unterberg, J. Barton, D. Rudakov, I. Bykov, C. Parish, R. Wilcox, C. Lasnier, T. Abrams, J. Watkins, D. Hillis, M. Bourham, Erosion characterization of SiC and Ti_3SiC_2 on DIII-D using focused ion beam micro-trenches, Nucl. Mater. Energy 19 (2019) 316–323, http://dx.doi.org/10.1016/j.nme.2019.02.036, URL https://www.sciencedirect.com/science/article/pii/S2352179118301947.

[5] T. Abrams, S. Bringuier, D. Thomas, G. Sinclair, S. Gonderman, L. Holland, D. Rudakov, R. Wilcox, E. Unterberg, F. Scotti, Evaluation of silicon carbide as a divertor armor material in DIII-D H-mode discharges, Nucl. Fusion 61 (6) (2021) 066005, http://dx.doi.org/10.1088/1741-4326/abecee.

[6] A. Yehia, R. Vaßen, R. Duwe, D. Stöver, Ceramic SiC/B_4C/TiC/C composites as plasma facing components for fusion reactors, J. Nucl. Mater. 233–237 (1996) 1266–1270, http://dx.doi.org/10.1016/S0022-3115(96)00155-9, URL https://www.sciencedirect.com/science/article/pii/S0022311596001559.

[7] L.B. Begrambekov, O.I. Buzhinskij, Features and advantages of boron carbide as a protective coating of the tokamak first wall, Plasma Devices Oper. 15 (3) (2007) 193–199, http://dx.doi.org/10.1080/10519990701450657.

[8] S. Kötterl, H. Bolt, H. Greuner, A. Huber, J. Linke, M. Mayer, A. Pospieszczyk, H. Renner, J. Roth, B. Schweer, G. Sergienko, D. Valenza, Development of thick B_4C coatings for the first wall of W7-X, Phys. Scr. 2001 (T91) (2001) 117, http://dx.doi.org/10.1238/Physica.Topical.091a00117.

[9] R. Tressler, Structural and thermostructural ceramics, in: K.J. Buschow, R.W. Cahn, M.C. Flemings, B. Ilschner, E.J. Kramer, S. Mahajan, P. Veyssière (Eds.), Encyclopedia of Materials: Science and Technology, Elsevier, Oxford, 2001, pp. 8913–8921, http://dx.doi.org/10.1016/B0-08-043152-6/01604-1, URL https://www.sciencedirect.com/science/article/pii/B0080431526016041.

[10] X. Su, Y. Bao, D. Wan, H. Zhang, L. Xu, S. Grasso, C. Hu, Thermal shock resistance of Ti_3SiC_2 ceramic under extremely rapid thermal cycling, J. Alloys Compd. 866 (2021) 158985, http://dx.doi.org/10.1016/j.jallcom.2021.158985, URL https://www.sciencedirect.com/science/article/pii/S0925838821003923.

[11] Y. Lee, T.J. McKrell, M.S. Kazami, Thermal shock fracture of silicon carbide and its application to LWR fuel cladding performance during reflood, Nucl. Eng. Technol. 45 (6) (2013) 811–820, http://dx.doi.org/10.5516/NET.02.2013.528, URL https://www.sciencedirect.com/science/article/pii/S1738573315301832.

[12] R. Maki, M. Fajar, J. Maletaskic, A. Gubarevich, K. Yoshida, T. Yano, T. Suzuki, T. Uchikoshi, Evaluation of thermal shock fracture resistance of B_4C/CNT composites with a high-frequency induction-heating furnace, Mater. Today: Proc. 16 (2019) 137–143, http://dx.doi.org/10.1016/j.matpr.2019.05.280, 6th International Symposium on Advanced Ceramics, URL https://www.sciencedirect.com/science/article/pii/S2214785319311265.

[13] Y. Yamauchi, T. Hino, Y. Hirohata, T. Yamashina, Hydrogen retention properties of SiC converted graphite, Vacuum 47 (6) (1996) 973–975, http://dx.doi.org/10.1016/0042-207X(96)00105-4, Proceedings of the 13th International Vacuum Congress and the 9th International Conference on Solid Surfaces, URL https://www.sciencedirect.com/science/article/pii/0042207X96001054.

[14] Y. Yamauchi, Y. Hirohata, T. Hino, T. Yamashima, T. Ando, M. Akiba, Hydrogen retention of B_4C converted graphite, J. Nucl. Mater. 220–222 (1995) 851–855, http://dx.doi.org/10.1016/0022-3115(94)00596-6, Plasma-Surface Interactions in Controlled Fusion Devices, URL https://www.sciencedirect.com/science/article/pii/0022311594005966.

[15] B. Buyuk, A.B. Tugrul, Gamma and neutron attenuation behaviours of boron carbide–silicon carbide composites, Ann. Nucl. Energy 71 (2014) 46–51, http://dx.doi.org/10.1016/j.anucene.2014.03.026, URL https://www.sciencedirect.com/science/article/pii/S0306454914001480.

[16] A. Shoshin, A. Burdakov, M. Ivantsivskiy, S. Polosatkin, M. Klimenko, A. Semenov, S. Taskaev, D. Kasatov, I. Shchudlo, A. Makarov, N. Davydov, Qualification of boron carbide ceramics for use in ITER ports, IEEE Trans. Plasma Sci. 48 (6) (2020) 1474–1478, http://dx.doi.org/10.1109/TPS.2019.2937605, URL https://ieeexplore.ieee.org/document/8827588.

[17] A. Shoshin, A. Burdakov, M. Ivantsivskiy, R. Reichle, V. Udintsev, J. Guirao, S. Pak, A. Zvonkov, D. Kravtsov, N. Sorokina, Y. Sulyaev, A. Listopad, D. Gavrilenko, A. Taskaev, E. Shabunin, V. Seryomin, S. Shiyankov, E. Zaytcev, P. Seleznev, A. Semenov, S. Polosatkin, S. Taskaev, D. Kasatov, I. Shchudlo, M. Bikchurina, V. Modestov, A. Smirnov, A. Pozhilov, A. Lobachev, I. Loginov, O. Shagniev, I. Kirienko, I. Buslakov, Integration of ITER diagnostic ports at the Budker institute, Fusion Eng. Des. 178 (2022) 113114, http://dx.doi.org/10.1016/j.fusengdes.2022.113114, URL https://www.sciencedirect.com/science/article/pii/S0920379622001144.

[18] U. Gökmen, Gamma and neutron shielding properties of B_4C particle reinforced Inconel 718 composites, Nucl. Eng. Technol. 54 (3) (2022) 1049–1061, http://dx.doi.org/10.1016/j.net.2021.09.028, URL https://www.sciencedirect.com/science/article/pii/S173857332100560X.

[19] A.W. Leonard, Edge-localized-modes in tokamaks, Phys. Plasmas 21 (9) (2014) 090501, http://dx.doi.org/10.1063/1.4894742.

[20] A. Vasilyev, A. Arakcheev, A. Burdakov, I. Bataev, I. Kandaurov, A. Kasatov, V. Kurkuchekov, V. Popov, A. Shoshin, Y. Trunev, L. Vyacheslavov, Continuous laser illumination for in situ investigation of tungsten erosion under transient thermal loads, Fusion Eng. Des. 146 (2019) 2366–2370, http://dx.doi.org/10.1016/j.fusengdes.2019.03.192, SI:SOFT-30, URL https://www.sciencedirect.com/science/article/pii/S0920379619305253.

[21] L. Vyacheslavov, A. Arakcheev, A. Burdakov, I. Kandaurov, A. Kasatov, V. Kurkuchekov, K. Mekler, V. Popov, A. Shoshin, D. Skovorodin, Y. Trunev, A. Vasilyev, Novel electron beam based test facility for observation of dynamics of tungsten erosion under intense ELM-like heat loads, AIP Conf. Proc. 1771 (1) (2016) 060004, http://dx.doi.org/10.1063/1.4964212, URL https://aip.scitation.org/doi/abs/10.1063/1.4964212.

[22] L.N. Vyacheslavov, A.A. Vasilyev, A.S. Arakcheev, D.E. Cherepanov, I.V. Kandaurov, A.A. Kasatov, V.A. Popov, A.A. Ruktuev, A.V. Burdakov, G.G. Lazareva, A.G. Maksimova, A.A. Shoshin, In-situ study of the processes of damage to the tungsten surface under transient heat loads possible in ITER, J. Nucl. Mater. 544 (2021) 152669, http://dx.doi.org/10.1016/j.jnucmat.2020.152669, URL https://www.sciencedirect.com/science/article/pii/S0022311520312770.

[23] L. Vyacheslavov, A. Arakcheev, A. Burdakov, I. Kandaurov, A. Kasatov, V. Kurkuchekov, K. Mekler, V. Popov, A. Shoshin, D. Skovorodin, Y. Trunev, A. Vasilyev, Observation of dust particles ejected from the tungsten surface by transient heat flux with small-angle scattering of cw laser light, Nucl. Mater. Energy 12 (2017) 494–498, http://dx.doi.org/10.1016/j.nme.2017.01.023, Proceedings of the 22nd International Conference on Plasma Surface Interactions 2016, 22nd PSI, URL https://www.sciencedirect.com/science/article/pii/S235217911630196X.

[24] A.A. Kasatov, A.S. Arakcheev, A.V. Burdakov, I.V. Kandaurov, V.V. Kurkuchekov, V.A. Popov, A.A. Shoshin, D.I. Skovorodin, Y.A. Trunev, A.A. Vasilyev, L.N. Vyacheslavov, Observation of dust particles ejected from tungsten surface under impact of intense transient heat load, AIP Conf. Proc. 1771 (1) (2016) 060007, http://dx.doi.org/10.1063/1.4964215.

[25] L.N. Vyacheslavov, A.S. Arakcheev, I.A. Bataev, A.V. Burdakov, I.V. Kandaurov, A.A. Kasatov, V.V. Kurkuchekov, V.A. Popov, A.A. Shoshin, D.I. Skovorodin, Y.A. Trunev, A.A. Vasilyev, Diagnostics of the dynamics of material damage by thermal shocks with the intensity possible in the ITER divertor, Phys. Scr. 93 (3) (2018) 035602, http://dx.doi.org/10.1088/1402-4896/aaa119.

[26] A. Vasilyev, A. Arakcheev, I. Bataev, V. Bataev, A. Burdakov, I. Kandaurov, A. Kasatov, V. Kurkuchekov, K. Mekler, V. Popov, A. Shoshin, D. Skovorodin, Y. Trunev, L. Vyacheslavov, In-situ imaging of tungsten surface modification under ITER-like transient heat loads, Nucl. Mater. Energy 12 (2017) 553–558, http://dx.doi.org/10.1016/j.nme.2016.11.017, Proceedings of the 22nd International Conference on Plasma Surface Interactions 2016, 22nd PSI, URL https://www.sciencedirect.com/science/article/pii/S235217911630117X.

[27] D. Cherepanov, A. Arakcheev, A. Burdakov, I. Kandaurov, A. Kasatov, V. Popov, A. Ruktuev, A. Vasilyev, L. Vyacheslavov, In situ method for studying stresses in a pulse-heated tungsten plate based on measurements of surface curvature, Nucl. Mater. Energy 26 (2021) 100919, http://dx.doi.org/10.1016/j.nme.2021.100919, URL https://www.sciencedirect.com/science/article/pii/S2352179121000156.

[28] A. Shoshin, A. Burdakov, M. Ivantsivskiy, M. Klimenko, S. Polosatkin, A. Semenov, Properties of boron carbide ceramics made by various methods for use in ITER, Fusion Eng. Des. 146 (2019) 2007–2010, http://dx.doi.org/10.1016/j.fusengdes.2019.03.088, SI:SOFT-30, URL https://www.sciencedirect.com/science/article/pii/S0920379619304090.

[29] H.O. Pierson, 8 - Characteristics and Properties of Silicon Carbide and Boron Carbide, in: H.O. Pierson (Ed.), Handbook of Refractory Carbides and Nitrides, William Andrew Publishing, Westwood, NJ, 1996, pp. 137–155, http://dx.doi.org/10.1016/B978-081551392-6.50009-X, URL https://www.sciencedirect.com/science/article/pii/B978081551392650009X.

[30] W. Martienssen, H. Warlimont, in: W. Martienssen, H. Warlimont (Eds.), Springer Handbook of Condensed Matter and Materials Data, Vol. 2005 XVIII, Springer, Berlin, 2005, p. 1120, http://dx.doi.org/10.1007/3-540-30437-1, 3-540-44376-2.

[31] V. Domnich, S. Reynaud, R.A. Haber, M. Chhowalla, Boron carbide: Structure, properties, and stability under stress, J. Am. Ceram. Soc. 94 (11) (2011) 3605–3628, http://dx.doi.org/10.1111/j.1551-2916.2011.04865.x, arXiv:https://ceramics.onlinelibrary.wiley.com/doi/pdf/10.1111/j.1551-2916.2011.04865.x, URL https://ceramics.onlinelibrary.wiley.com/doi/abs/10.1111/j.1551-2916.2011.04865.x.

[32] R.V. Goldstein, N.M. Osipenko, About compression fracture, Phys. Mesomech. 22 (6) (2019) 439–455, http://dx.doi.org/10.1134/S1029959919060018.

[33] R.J. Martin III, Time-dependent crack growth in quartz and its application to the creep of rocks, J. Geophys. Res. (1896-1977) 77 (8) (1972) 1406–1419, http://dx.doi.org/10.1029/JB077i008p01406, arXiv:https://agupubs.onlinelibrary.wiley.com/doi/pdf/10.1029/JB077i008p01406, URL https://agupubs.onlinelibrary.wiley.com/doi/abs/10.1029/JB077i008p01406.

[34] L.D. Landau, E.M. Lifshitz, A.M. Kosevich, L.P. Pitaevskii, Theory of Elasticity, Vol. 7, Elsevier, 1986, URL https://books.google.ru/books/about/Theory_of_Elasticity.html?hl=de&id=tpY-VkwCkAIC&redir_esc=y.

[35] A. Loarte, G. Saibene, R. Sartori, V. Riccardo, P. Andrew, J. Paley, W. Fundamenski, T. Eich, A. Herrmann, G. Pautasso, A. Kirk, G. Counsell, G. Federici, G. Strohmayer, D. Whyte, A. Leonard, R.A. Pitts, I. Landman, B. Bazylev, S. Pestchanyi, Transient heat loads in current fusion experiments, extrapolation to ITER and consequences for its operation, Phys. Scr. 2007 (T128) (2007) 222, http://dx.doi.org/10.1088/0031-8949/2007/T128/043.

[36] P.E. Johnson, D.P. DeWitt, R.E. Taylor, Method for measuring high temperature spectral emissivity of nonconducting materials, AIAA J. 19 (1) (1981) 113–120, http://dx.doi.org/10.2514/3.50929.

[37] R.J. Hayes, Determination of the Emissivity of Materials, Tech. Rep. PWA-2163, Pratt and Whitney Aircraft East Hartford, CT, United States, 1962, pp. 113–120, URL https://ntrs.nasa.gov/citations/19630008443.

[38] J.I. Larruquert, A.P. Pérez-Marín, S. García-Cortés, L.R. de Marcos, J.A. Aznárez, J.A. Méndez, Self-consistent optical constants of sputter-deposited B_4C thin films, J. Opt. Soc. Amer. A 29 (1) (2012) 117–123, http://dx.doi.org/10.1364/JOSAA.29.000117.

[39] J.H. Yu, R.P. Doerner, T. Dittmar, T. Höschen, T. Schwarz-Selinger, M.J. Baldwin, ITER-relevant transient heat loads on tungsten exposed to plasma and beryllium, Phys. Scr. 2014 (T159) (2014) 014036, http://dx.doi.org/10.1088/0031-8949/2014/T159/014036.

[40] V. Soukhanovskii, R. Bell, A. Diallo, S. Gerhardt, S. Kaye, E. Kolemen, B. LeBlanc, A. McLean, J. Menard, S. Paul, M. Podesta, R. Raman, D. Ryutov, F. Scotti, R. Kaita, R. Maingi, D. Mueller, A. Roquemore, H. Reimerdes, G. Canal, B. Labit, W. Vijvers, S. Coda, B. Duval, T. Morgan, J. Zielinski, G. De Temmerman, B. Tal, Advanced divertor configurations with large flux expansion, J. Nucl. Mater. 438 (2013) S96–S101, http://dx.doi.org/10.1016/j.jnucmat.2013.01.015, Proceedings of the 20th International Conference on Plasma-Surface Interactions in Controlled Fusion Devices, URL https://www.sciencedirect.com/science/article/pii/S0022311513000238.

[41] G. Pintsuk, W. Kühnlein, J. Linke, M. Rödig, Investigation of tungsten and beryllium behaviour under short transient events, Fusion Eng. Des. 82 (15) (2007) 1720–1729, http://dx.doi.org/10.1016/j.fusengdes.2007.06.030, Proceedings of the 24th Symposium on Fusion Technology, URL https://www.sciencedirect.com/science/article/pii/S0920379607003341.

[42] A.D. Polyanin, Handbook of Linear Partial Differential Equations for Engineers and Scientists, first ed., Chapman & Hall/CRC, 2002, http://dx.doi.org/10.1201/b19056.

[43] R. Morell, 1 - An introduction for the engineer and designer, in: Handbook of Properties of Technical and Engineering Ceramics, National Physical Laboratory, London, 1985.

[44] A. Suslova, O. El-Atwani, D. Sagapuram, S.S. Harilal, A. Hassanein, Recrystallization and grain growth induced by ELMs-like transient heat loads in deformed tungsten samples, Sci. Rep. 4 (6845) (2014) http://dx.doi.org/10.1038/srep06845.

[45] M. Richou, A. Durif, M. Lenci, M. Mondon, M. Minissale, L. Gallais, G. Kermouche, G. De Temmerman, Recrystallization at high temperature of two tungsten materials complying with the ITER specifications, J. Nucl. Mater. 542 (2020) 152418, http://dx.doi.org/10.1016/j.jnucmat.2020.152418, URL https://www.sciencedirect.com/science/article/pii/S0022311520310266.

[46] A. Huber, A. Arakcheev, G. Sergienko, I. Steudel, M. Wirtz, A.V. Burdakov, J.W. Coenen, A. Kreter, J. Linke, P. Mertens, V. Philipps, G. Pintsuk, M. Reinhart, U. Samm, A. Shoshin, B. Schweer, B. Unterberg, M. Zlobinski, Investigation of the impact of transient heat loads applied by laser irradiation on ITER-grade tungsten, Phys. Scr. 2014 (T159) (2014) 014005, http://dx.doi.org/10.1088/0031-8949/2014/T159/014005.

[47] F. Maviglia, C. Bachmann, G. Federici, T. Franke, M. Siccinio, R. Albanese, R. Ambrosino, W. Arter, R. Bonifetto, G. Calabrò, R. De Luca, L.E.D. Grazia, E. Fable, P. Fanelli, A. Fanni, M. Firdaouss, J. Gerardin, R. Lombroni, M. Mattei, M. Moscheni, W. Morris, G. Pautasso, S. Pestchanyi, G. Ramogida, M.L. Richiusa, G. Sias, F. Subba, F. Villone, J.-H. You, Z. Vizvary, Integrated design strategy for EU-DEMO first wall protection from plasma transients, Fusion Eng. Des. 177 (2022) 113067, http://dx.doi.org/10.1016/j.fusengdes.2022.113067, URL https://www.sciencedirect.com/science/article/pii/S0920379622000679.